The Electrochemical Society
Advancing solid state & electrochemical science & technology

The Negative Impact of Transition Metal Migration on Oxygen Redox Activity of Layered Cathode Materials for Na-Ion Batteries

The Negative Impact of Transition Metal Migration on Oxygen Redox Activity of Layered Cathode Materials for Na-Ion Batteries

Hayley Hirsh,[=] Yixuan Li,[=] Ju-Hsiang Cheng, Ryosuke Shimizu, Minghao Zhang,[*] Enyue Zhao, and Ying Shirley Meng[**,z]

Department of NanoEngineering, University of California San Diego, La Jolla, California 92093-0448, United States of America

Rechargeable sodium ion batteries with high energy density are a promising technology to address the demand for grid storage. Cathode materials with oxygen redox activity exhibit higher energy density than expected from Na-ion removal and charge compensation solely by transition metal redox. One strategy to enable oxygen redox in materials is to alter the oxygen environment through transition metal layer ordering. In this work, we report the investigation of oxygen redox activity induced by transition metal ordering in P2-type $Na_{0.8}Li_{0.12}Ni_{0.22}Mn_{0.66}O_2$ cathode synthesized by carbonate co-precipitation. Irreversible oxygen activity was observed and correlated with Ni migration that resulted in the loss of transition metal ordering in the structure. Calculated density of states shows that after Ni migration, the number of unoccupied states of O above Fermi level decreases, inhibiting the reduction of oxygen during sodiation. This paper provides insights on how Ni migration has a detrimental effect on transition metal ordering and reversibility of oxygen redox at high voltage.
© 2021 The Electrochemical Society ("ECS"). Published on behalf of ECS by IOP Publishing Limited. [DOI: 10.1149/1945-7111/abf96e]

Sodium ion batteries (NIBs) are emerging as a promising grid storage technology due to its low cost of energy.[1] Various types of cathode materials have been investigated for NIBs, including layered oxides, poly-anionic frameworks, hexacyanoferrates, and organics.[2–7] Among the sodium cathode materials, layered sodium transition metal oxides, Na_xTMO_2 (TM = Mn, Fe, Ni, Cu, Ti, Co, Cr or mixture of elements), are strong contenders due to their high volumetric energy densities.[8,9] Specifically, P2-type Na_xTMO_2 have enhanced electrochemical performance due to minimal structural changes during cycling.[10–12] In these structures, P2 refers to the stacking sequence of the layered oxide, as introduced by Delmas et al.[13] In this notation, the letter indicates the coordination environment of the sodium ion (P for prismatic, O for octahedral, or T for tetragonal) and the number indicates the quantity of sheets within a unit cell (1, 2, or 3). Even with the relative high capacity of P2 cathodes compared to other sodium cathode materials, there is still a need to further increase the capacity at high voltage to optimize their energy density for use in grid storage.

In conventional cathode materials, cationic redox (Mn^{3+}/Mn^{4+}, Ni^{2+}/Ni^{4+}, Co^{3+}/Co^{4+}, etc.) is utilized to maintain a charge balance as Li^+/Na^+ ions leave the compound.[14,15] The capacity of these cathode materials is limited by the cationic redox. Recently, oxygen redox has been accessed for cathodes in LIBs to increase their capacity beyond the "theoretical" capacities based on cationic redox.[16–19] This is observed in lithium rich layered oxide (LRLO) cathode materials with the composition, $xLi_2TMO_3·(1 − x)LiTMO_2$ (TM = 3d, 4d, and 5d transition metals) as a nano composite. During charge and discharge, LRLO materials experience the redox of TMs with simultaneous extraction/insertion of Li ions similar to classical layered NMC materials. However, above 4.3 V, LRLO materials also experience redox activity of oxygen, which contributes significantly to the large capacities of LRLO.[20,21] In these materials, the excess lithium, which has a similar radius to TMs, sits in the TM layers. This creates an environment where the Li-O-Li bond has a lone-pair of oxygen electrons that are oxidized for charge compensation during Li-extraction.[22] In the voltage curve, this mechanism has a characteristic plateau at high voltage. Within lithium rich cathodes, ordering of the atoms in the TM layer is commonly seen

and contributes to the activation of oxygen activity.[23] For oxygen redox to be activated in layered cathode materials, pure oxygen O (2p) states are required to be slightly below the Fermi level.[18] This condition can be triggered by the O-TM stoichiometry and bonding environment.[20,24–26]

In sodium 3d TM layered cathode materials, oxygen activity has been observed in two cases. In the first case, sodium cathode materials are substituted with Li, such as $Na_{0.6}Li_{0.2}Mn_{0.8}O_2$ and $Na_{0.72}Li_{0.24}Mn_{0.76}O_2$.[27,28] The oxygen redox mechanism for these Li-rich Na-ion layered compounds is proposed to be identical to the one for Li_2MnO_3 and Li-rich Li-ion layered compounds, where the lone-pair oxygen electrons in the Na (Li)-O-Li bond are oxidized for charge compensation during Na (Li)-extraction. However, the substitution of Li is not necessary to create such O 2p nonbonding orbitals.[29] In fact, similar oxygen redox behavior has also been reported in Mg-substituted samples such as $Na_{2/3}Mg_{0.28}Mn_{0.72}O_2$.[30] In the second case, using a similar concept, under coordinated oxygen caused by vacancies in the TM layer, can trigger oxygen redox in the following compounds: $Na_{4/7}Mn_{6/7}O_2$, $Na_{0.78}Ni_{0.23}Mn_{0.69}O_2$, and $Na_{0.653}Mn_{0.929}O_2$.[31–33] A table of NIB cathodes that are reported to have oxygen redox are shown in SI Table I. It is notable that most of the compounds containing Ni do not have reversible oxygen redox. Specifically, the high voltage plateaus in these compounds lack reversibility even if the cation redox processes remain reversible. This leads to the question: does Ni play a role in irreversible oxygen redox, and if so, what is the mechanism of irreversibility?

While Ni has not been identified as the origin of irreversible oxygen redox in NIBs, Ni has been reported as a problematic component of Li-rich disordered rock salt cathodes.[34] In these compounds, Ni, in contrast with Mn, induces irreversible oxygen redox through oxygen gas release. Ni migration, in these disorder rock salt cathodes, could play a role in the irreversible oxygen redox processes, where Ni migration within the structure could alter the bonding environment of oxygen. This makes oxygen reduction unfavorable during discharge, therefore inhibiting the oxygen redox reversibility. Additionally, the negative impacts of TM migration were previously reported for Li-rich layered TM oxide cathode materials.[35] There are several unfavorable electrochemical properties in Li-rich layered oxides, such as the open-circuit voltage hysteresis, that arise from the drastic change in the local oxygen coordination environments induced by TM migration. Furthermore, in oxygen redox active compounds that rely on TM layer ordering

[=]These authors contributed equally to this work.
[*]Electrochemical Society Student Member.
[**]Electrochemical Society Fellow.
[z]E-mail: shirleymeng@ucsd.edu

for suitable oxygen bonding environments, TM migration could disrupt the ordered structure and inhibit further oxygen redox. There are examples of such phenomena in both Li-ion layered cathode and Na-ion layered compounds.[35,36]

In this work, we explore a pure phase spherical meso-structure controlled P2-type $Na_{0.8}Li_{0.12}Ni_{0.22}Mn_{0.66}O_2$ (NLNMO) with TM layer ordering that was synthesized using a carbonate co-precipitation method. In NLNMO, a plateau region is observed at high voltages during the first charge. Superlattice peaks are seen in the X-ray diffraction pattern, which indicate TM metal layer ordering. This ordering can potentially alter the environment of the oxygen atoms and this allows oxygen redox to become favorable. After the first electrochemical cycle, the TM ordering disappears along with the oxygen plateau. Ni migration is identified as the cause of the irreversible oxygen redox by disrupting the TM honeycomb ordering and inhibiting oxygen reduction during sodiation. These mechanisms could have a profound impact on the future design of sodium cathode materials. By controlling the reversibility of oxygen activity, the energy density of sodium cathode materials can be dramatically increased.

Experimental

Materials preparation.—Stoichiometric amounts of the precursor, $Ni(NO_3)_2 \cdot 6H_2O$ and $Mn(NO_3)_2 \cdot 4H_2O$ (Ni:Mn = 1:3 in molar ratio), were dissolved in DI water for a total concentration of 1 M. The TM nitrate solution and an aqueous solution of 0.2 M Na_2CO_3 were separately pumped into a reaction vessel to maintain the pH value at 7.8. The obtained mixture was aged at 80 °C for 12 h in a sealed vessel. The resulting spherical $Ni_{1/4}Mn_{3/4}CO_3$ was washed with deionized water to remove residual Na^+ and NO_3^{2-} and then dried at 80 °C overnight. The obtained $Ni_{1/4}Mn_{3/4}CO_3$ powder was mixed with a 5% excess stoichiometric ratio of Na_2CO_3 and Li_2CO_3. The mixture was calcinated at 900 °C for 15 h in air.

Materials characterization.—The crystal structures were characterized by X-ray diffraction (XRD) using a Rigaku Smartlab XRD with a copper Kα source. Rietveld refinement was applied to the obtained diffraction pattern using FullProf Software. The morphology and meso-structure of the particles were identified using a Ziess Sigma 500 scanning electron microscope (SEM) with an accelerating voltage of 1 keV. Cross-section of the particles was acquired and imaged using a FEI Scios DualBeam focused ion beam (FIB)/SEM. Inductively coupled plasma optical emission spectroscopy (ICP-OES) was performed using a Perkin Elmer 3000 optical emission plasma spectrometer.

X-ray absorption spectroscopy (XAS) spectra were performed at National Synchrotron Radiation Research Center (NSRRC) in Taiwan. Ni and Mn K-edges hard X-ray absorption spectra were collected at the beamline BL17C by using the transmission mode. Ni and Mn reference foils were measured simultaneously to calibrate energy for each scan. Spectra were analyzed using the Demeter XAS

software package. O K-edge spectra were performed at soft XAS beamline (BL20A) with a fluorescence yield (FY) mode in an ultrahigh-vacuum (UHV) chamber. Ex situ XAS samples were prepared by charging/discharging 2032 cells at a rate of C/10 as described in the electrochemical characterization section and then disassembled. The electrodes were rinsed with propylene carbonate (PC) and dried in an Ar-filled glovebox.

Operando synchrotron XRD (sXRD) and pair distribution function (PDF) data were collected at 11-ID-B in Advanced Photon Source (APS) at Argonne National Laboratory with a wavelength of 0.2115 Å. An AMPIX cell was assembled with a NLNMO cathode and Na metal anode and cycled at a rate of C/15 (1C = 118 mA g^{-1}) between 2.0 V to 4.4 V. GSAS-2[37] was used to extract the XRD pattern as well as to perform Rietveld refinement to the collected data. PDF data was analyzed through PDF suite and PDF gui.[38] The Q-max used for the Fourier transfer is 20.5 Å^{-2}. In the PDF refinement, the instrumental parameters Qdamp and Qbroad were set to be 0.0251 Å^{-2} and 0.0199 Å^{-2} separately.

Electrochemical characterization.—Composite cathode electrodes were prepared by mixing a slurry of NLNMO, acetylene carbon black, and polyvinylidene fluoride (PVDF) in a weight ratio of 8:1:1, with n-methyl-2-pyrrolidone as the solvent. The slurry was cast on aluminum foil and dried under vacuum at 80 °C overnight. The electrodes were assembled in 2032 coin cells in an argon filled glove box (H_2O < 0.1 ppm) with Na metal as the counter electrode, glass fiber GF/D (Whatman) as the separator, and 70 μl of 1 M $NaPF_6$ in PC as the electrolyte. The coin cells were allowed to rest 8 h before electrochemical testing on an Arbin battery cycler. The C-rates were calculated with a theoretical specific capacity of 118 mAh/g and the voltage range was maintained between 2–4.4 V.

Computation study.—The electronic structure of NLNMO was investigated in the spin polarized GGA+U approximation to Density Functional Theory (DFT). Projector augmented-wave method (PAW) pseudopotentials were employed, as implemented, in the Vienna Ab initio Simulation Package (VASP).[39] The Perdew-Bruke-Ernzerhof (PBE) exchange correlation and a plane-wave representation for the wavefunction[40] were used, where a cut-off energy was set at 450 eV. The Brillouin zone was sampled with a k-points mesh of 5 × 4 × 4 for structural relaxations and 10 × 8 × 8 for density of states (DOS) calculations. Effective U values used through all the calculations were 3.9 for Mn and 6.2 for Ni, which are adopted from recent studies in the Materials Project.[41] $Na_{14}Mn_8Ni_4Li_2O_{28}$ was used as a starting structure and density of states were calculated at the structure of $Na_{3/14}$ with Li vacancy.

Results and Discussion

Pristine P2-$Na_{0.8}Li_{0.12}Ni_{0.22}Mn_{0.66}O_2$ (NLNMO) was prepared by a modified meso-structure controlled co-precipitation method. Unlike previously reported methods which result in a hexagonal
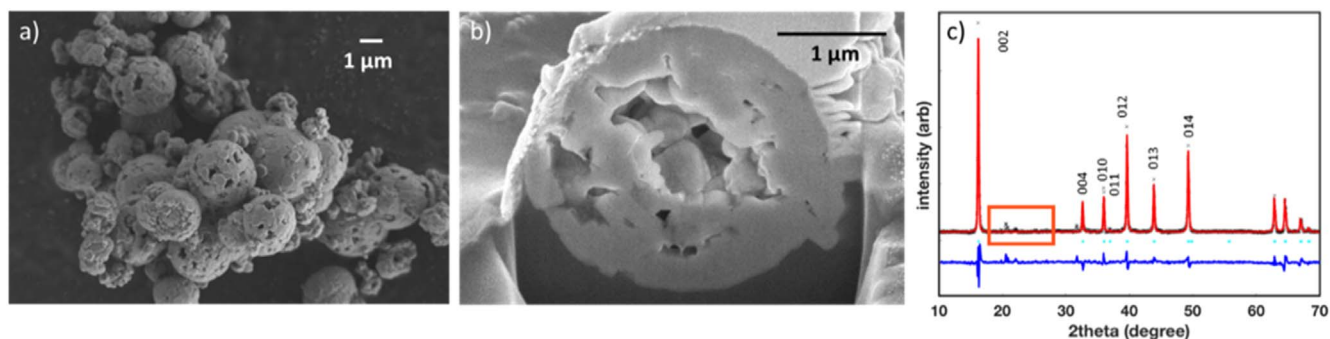

Figure 1. (a) SEM image of NLNMO powder with primary hexagonal particles of 100–500 nm in diameter and secondary spherical particles of 1–3 μm in diameter. (b) A cross section of an NLNMO particle with large pores in its secondary structure. (c) XRD data of NLNMO with superlattice peaks highlighted with an orange square.

particle morphology, this modified co-precipitation yields spherical secondary particles 2–3 μm in diameter comprised of hexagonal primary particles 100–500 nm in diameter (Fig. 1a).[42,43] A cross section of a secondary particle is shown in Fig. 1b. The secondary particle contains pores that are beneficial for electrolyte penetration into the bulk of this material. Electrolyte penetration into the bulk of the material enables all of the primary particles in the meso-structure to be electrochemically active. The spherical shape of the carbonate precursors (SI Fig. 1 (available online at stacks.iop.org/JES/168/040539/mmedia)) is retained in the final product of NLNMO.

The composition of NLNMO was confirmed with ICP-OES (SI Table II). NLNMO diffraction peaks can be well indexed to space group $P6_3/mmc$ (Fig. 1c) with Rietveld refinement results (SI Table II) confirming that the material is a pure phase P2 layered material. A P2-type layered structure, as defined by Delmas et al., has ABBA oxygen stacking sequence where Na ions are located in the trigonal prismatic sites.[13] Additionally, the XRD data of NLNMO have small but noticeable peaks between 19–28 degrees that do not correspond to the otherwise pure P2 phase. These peaks indicate superlattice ordering in the TM layer. A. R. Armstrong et al. reported that these peaks correspond to ordering of Li/Mn/Ni in the TM layer.[44] When the radii of the ions in the TM have a difference of 15% or larger, TM layer ordering is favorable.[45] The ionic radii of the ions in the TM layer fit this criterial Li$^+$(0.76 Å), Ni^{2+}(0.69 Å), and Mn^{4+}(0.53 Å).[46] Although such TM ordering is thermodynamically favorable, it may be dependent on the synthesis method. This may explain why some previous reported sodium layered cathode materials containing Li/Ni/Mn do not have TM layer ordering.[47]

To explore the electrochemical properties of NLNMO, half cells, with sodium metal as the anode, were prepared and cycled in galvanostatic mode at various rates, C/1, C/10, and C/50 where the theoretical capacity is 118 mAh g^{-1} based on the Ni^{2+}/Ni^{4+} redox (Fig. 2). At a rate of C/50, there is a prominent voltage plateau in the first charge voltage curve between 4.2–4.4 V (Fig. 2a). This plateau increases the first charge capacity from 118 mAh g^{-1} to 180 mAh g^{-1}. The extent of the high voltage plateau during the first charge is rate dependent. At a faster rate of C/10 (Fig. 2b), the high voltage plateau is reduced but still contributes ~20 mAh g^{-1} to the first charge capacity. For a fast rate of C/1 (Fig. 2c) no plateau is observed in first charge. Given the capacity limitations of the Ni redox, high charge capacity at slow rates cannot solely be the result of the Ni^{2+}/Ni^{4+} redox. Because the high voltage plateau is rate dependent and does not contribute to the discharge capacity or subsequent cycles, irreversible oxygen redox could be the origin. Furthermore, in previous literature of NLNMO, neither a high voltage plateau during the first charge nor superlattice ordering in the XRD data were reported.[43] The TM ordering in NLNMO of this study may alter the oxygen bonding environment and this triggers oxygen redox. The extra capacity disappears for subsequent cycles at all rates. This suggests that the environment of the oxygen atoms likely changes after the first charge, which inhibits further oxygen

redox. The environment and oxidation states of NLNMO are thus explored to determine the source of the high voltage plateau.

To investigate the orgin of high-capacity in the meso-structure controlled NLNMO, the evolution of the oxidation state and local environment of Mn, Ni, and O were probed by XAS. Ex situ samples of NLNMO were prepared at six different states of charge and discharge as shown in Fig. 2b, including pristine, charging to 3.2 V, 4.2 V and 4.4 V (red circles and prefixed as "C"), and then discharging to 2.9 V and 2.0 V (blue circles and prefixed as "D"). X-ray absorption near edge spectroscopy (XANES) spectra at Ni K-edge and Mn K-edge are shown in Figs. 3a and 3b. Based on comparison with standard references (NiO, MnO, Mn$_2$O$_3$, and MnO$_2$), the pristine NLNMO is suggested to predominantly consist of Mn^{4+} and Ni^{2+}. The Mn K-edge shifts negligibly during the first cycle (Fig. 3e, signifying that Mn does not participate in the electrochemical charge transfer reaction. On the other hand, Ni K-edge shifts to higher energy when charged to 4.2 V, indicating that Ni^{2+} has been oxidized to Ni^{4+} (Fig. 3d). The Ni K-edge at 4.4 V is shifted to lower energy than the edge at 4.2 V. This implies that between 4.2 V and 4.4 V, Ni is slightly reduced even though that region of the voltage curve delivers 30 mAh g^{-1} of capacity. Given that Ni^{2+}/Ni^{4+} redox occurs below 4.2 V, a different charge transfer mechanism must contribute to the capacity in the high voltage plateau between 4.2–4.4 V. This high voltage mechanism is not Mn redox because, based on the XANES Mn K-edge observations, Mn^{4+} is redox inactive. Therefore, it is likely that oxygen participates in the high voltage charge compensation process, similar to other layered sodium cathode materials with oxygen redox activities.[30,32] To further explore this charge compensation process in NLNMO at high voltage, the O K-edge was used to investigate oxygen's participation in the redox mechanism.

The pre-edge peak position and intensities of the O K-edge XANES spectra can provide structural and chemical bond information between the oxygen and transition metal species, as shown in Fig. 3c. The O K-edge can be divided into two regions: the pre-edge peaks below 535 eV, which correspond to electronic transitions from the O 1 s state to the O 2p-TM 3d hybridized state, and the broad peaks above 535 eV, which correspond to transitions to O 2p-TM 4sp hybridization states.[48] For the lower energy peaks, the possible O K-edge sXAS transitions anticipated for these states are shown in SI Fig. 2. The dominant TM ions in NLNMO at 4.2 V are Mn^{4+} (3d^3) and Ni^{4+} (3d^6).[16] There are seven possible sXAS transitions associated with Mn^{4+}: three spin-down t$_{2g}$, two spin-up e$_g$, and two spin-down e$_g$ For Ni^{4+}, there are four possible sXAS transitions: two spin-up e$_g$ and two spin-down e$_g$ transitions. Given that per unit formula Mn^{4+} = 0.66 and Ni^{4+} = 0.22, Mn^{4+} accounts for 84% of the expected sXAS transitions to the unoccupied states and thus dominates the spectrum. The peaks around 529 eV and 532 eV can be assigned to the unoccupied hybridized orbitals of O 2p-TM t$_{2g}$ and O 2p-TM e$_g$ respectively.[47] The O K-edge spectrum of pristine NLNMO shows a peak at 534 eV, which is ascribed to the unoccupied hybridization orbital of O 2p-Na 3p, and its intensity
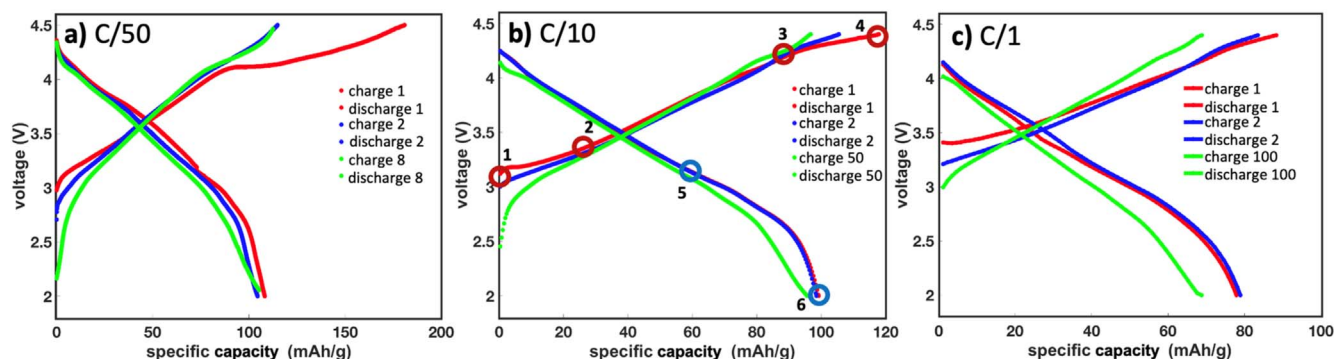
Figure 2. Voltage profiles of NLNMO half cells cycled at rates of (a) C/50, (b) C/10, and (c) C/1. In voltage profile (b) the numbers mark the voltages where ex situ XAS data was recorded.
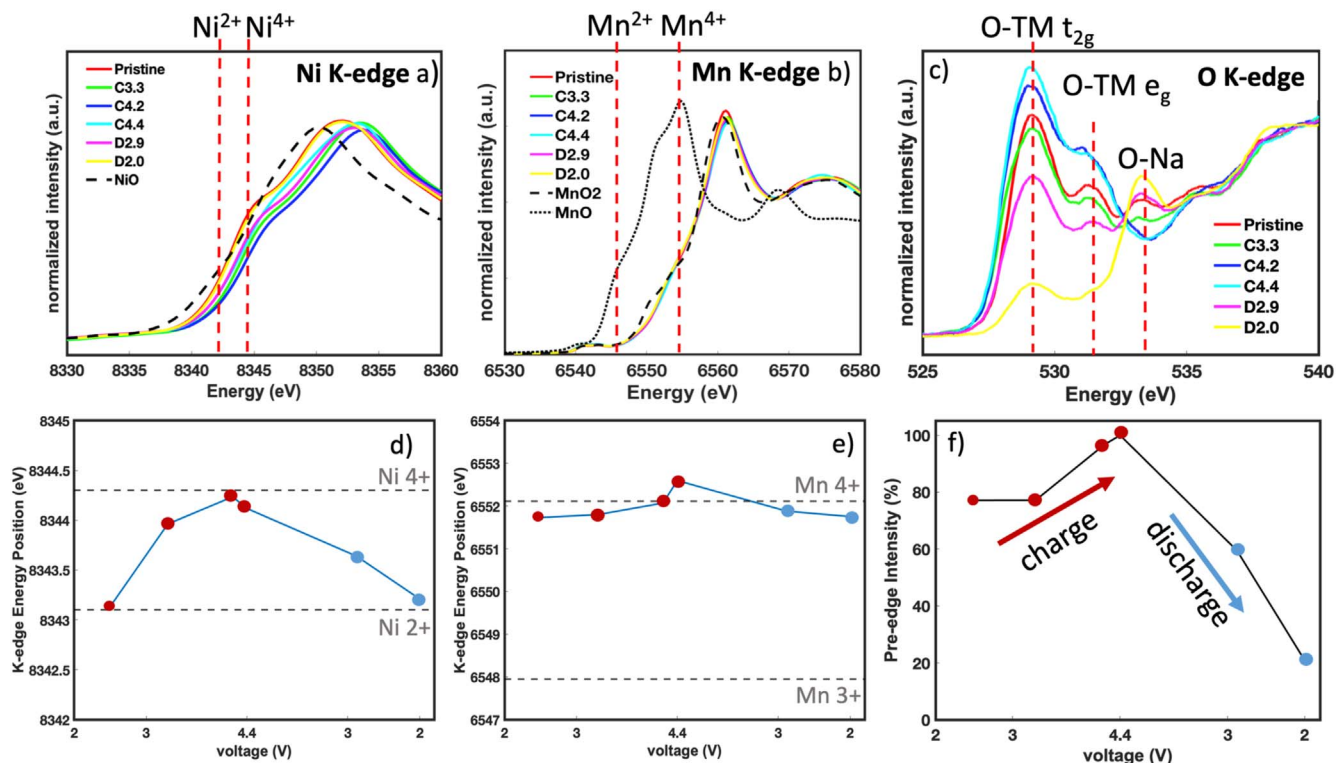
Figure 3. The ex situ XANES spectra and respective positions of the (a), (d) Ni K-edge, and (b), (e) Mn K-edge of NLNMO at different states of charge. (c) ex situ XANES spectra of the O K-edge (FY mode) and the (f) integrated pre-edge intensity of the O K-edge at different states of charge.

reflects the amount of Na in the lattice.[49] As the NLNMO is charged, the O 2p-Na 3p signal diminishes, in agreement with desodiation. The peak intensity of O 2p-TM t_{2g} and e_g increase upon charging, which indicates hole generation in the O 2p-TM orbital. Hole generation in the O 2p-TM orbital could be created to compensate the positive charge of the Na^+ ion leaving the cathode structure. Although O K-edge alone cannot prove the electron holes in oxygen are present due to strong hybridization of O 2p-TM, it is highly likely given the observations that Mn remains in the 4+ state and Ni becomes slightly reduced at the fully charged state.[42]

On discharge, the peaks due to O 2p-TM t_{2g} and O 2p-TM e_g decrease and the O 2p-Na 3p peak increases upon sodiation. At the fully discharged state (2.0 V), the O-TM t_{2g} and O-TM e_g signals are minimized, with lower intensity than the pristine state. This may indicate an irreversible change in the TM-O bond, which may inhibit further oxygen redox. Oxygen loss from the lattice during the first charge is common in oxygen redox cathode materials and may contribute to the irreversible capacity loss seen in NLNMO.[50] The Ni K-edge is shifted to lower energy upon discharge and at the fully discharged state, the Ni ions are reduced back to their divalent state. This demonstrates that the Ni redox reaction is completely reversible, unlike the case of irreversible oxygen redox. Mn K-edge shifts negligibly during discharge, implying that it stays electrochemically inactive.

The structure changes of NLNMO during the first electrochemical cycle were explored with operando sXRD shown in Fig. 4. The operando cell has a specific charge capacity of 165 mAh g^{-1} and a specific discharge capacity of 113 mAh g^{-1}. The collected sXRD patterns over cycling were plotted into a contour plot and shown in Fig. 4b. All the peaks in the data can be well indexed to $P6_3/mmc$ space group, except for the peak at $2\theta = 2.46°$. This peak is at the position of Li_2MnO_3 (0 2 0) peak and is known as a superlattice peak in layered structures and corresponds to a honeycomb superstructure within the TM layer.[51,52] After the initial cycle, the XRD patterns indicate that the P2 structure remains with slight peak position shifts, which will be quantified with lattice

parameter changes later. A magnified region of the (002) peak and the superlattice peak is presented in Fig. 4c, where a decrease of the superlattice peak intensity can be observed during the first cycle. As a comparison, the (002) peak maintains the same intensity level during the whole cycle, with the peak shifting in both charge and discharge process. The decrease of superlattice peak after cycling indicates severe degradation of the TM ordering in the TM layer in NLNMO. Such degradation corresponds to the loss of the honeycomb superstructure within the TM layer that may be caused by migration of TM ions in the structure.[36,44]

The changes in the overall crystal structure are characterized with a/c lattice parameters change through Rietveld refinement (Figs. 4d, 4e). The pristine material has a lattice a parameter of 2.89 Å that shrinks to 2.83 Å at the end of the first charge. The reduction in the a lattice parameter corresponds to shortening TM-TM bonds due to oxidation of the TM upon charging.[43] During the discharge, the a lattice parameter increases due to reduction of the TMs and returns to 2.86 Å at the end of the discharge. Lattice parameter a cannot fully return to its initial state due to decreased ordering of the TM layer which inhibits bond lengths from returning to their original state.

The changes in the c lattice parameter over cycling are more complex than the changes in lattice a. The c lattice parameter is 11.05 Å in the pristine state and it increases to a maximum of 11.32 Å around 4.05 V in the charging, and then decreases to 11.29 Å at the end of charge. The initial increase in the c lattice parameter is due to the increased electrostatic repulsion between the negatively charged oxygen layers along with the removal of the positively charged sodium ions. The following decrease of the c lattice parameter from 4.05 V to 4.4 V could be due to the oxidation of oxygen which reduces the magnitude of repulsion between the oxygen layers. The magnitude of repulsion is decreased due to charge of oxygen reducing from −2 to a value closer to −1. During the discharge, the c lattice parameter increases first to 11.30 Å around 3.80 V and decreases to 11.18 Å at the end of discharge. Similar to the charge process, the oxidized lattice oxygen could
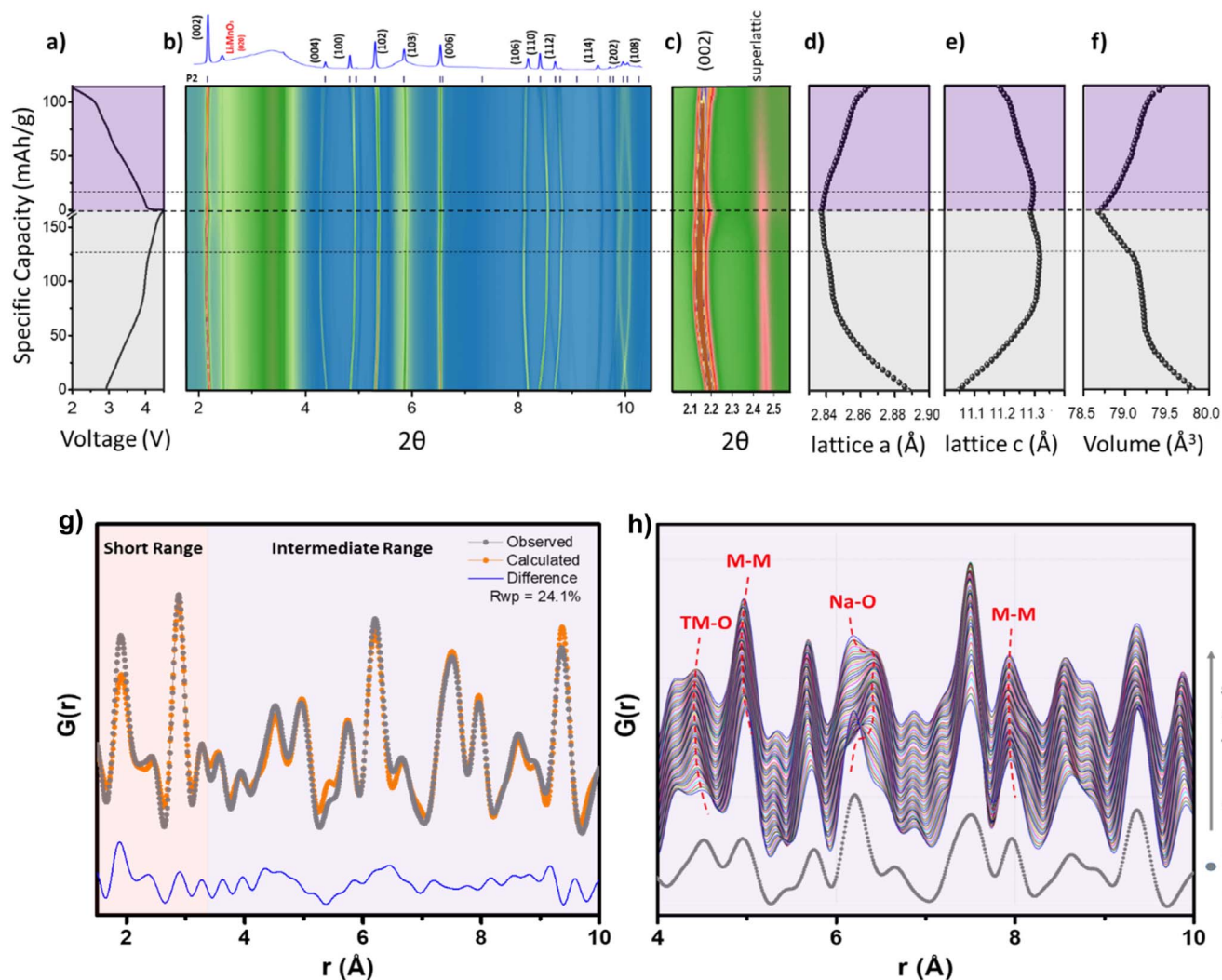
Figure 4. (a) Voltage profile of the initial cycle of NLNMO in the operando sXRD data collection; (b) contour plot of the sXRD pattern obtained over cycling; (c) magnified (002) peak and superlattice peak region; (d) lattice *a*, (e) lattice *c* and (f) unit cell volume obtained from Rietveld refinement; (g) refinement of PDF pattern of pristine NLNMO powder, detailed refinement results are listed in SI Table III; (h) operando PDF of NLNMO during first cycle between 2.0–4.4 V.

initially be reduced, which increases the repulsion between the layers until 3.80 V and where the reduction of electrostatic repulsion by the addition of sodium ions reduces the *c* lattice parameter. And similar to *a* lattice parameter, the *c* lattice parameter cannot fully return to its initial state due to irreversible changes in TM layer ordering. The volume of NLNMO unit cell was calculated from refined *a* and *c* lattice parameters. The initial unit cell volume is 79.81 Å^3 and decreases to 78.68 Å^3 at the end of charge. It recovers in the discharge process and increases back to 79.45 Å^3 in the end of discharge. Similar to lattice *a* and lattice *c*, the shrinking of the total volume cannot fully recover even at the end of discharge, indicating the loss of honeycomb ordering within the TM layer. The initial lattice parameters are essentially identical to the parameters of previously reported structures but have larger changes during the charging and do not return to their initial states, indicating a different mechanism of redox reactions in the material reported here.[53]

The overall structure of NLNMO was explored with sXRD and the loss of TM ordering within the TM layer is observed with the severe decrease of superlattice peak. The local environment of NLNMO was probed with pair distribution function (PDF) shown in Figs. 4g, 4h. PDF results of pristine NLNMO powder were refined through small box (unit-cell based) refinements. The observed PDF pattern matches the calculated pattern from *P*6$_3$/*mmc* space group. The *a* and *c* lattice parameters obtained from PDF refinement (a =

2.88 Å, c = 11.00 Å) are consistent with the Rietveld refined values from sXRD. The anisotropic thermal displacement parameter was modeled as U12 in the PDF refinement and shows an increase in the refinement liability, which indicates anisotropic behavior of this material.

The changes of local environment in NLNMO over cycling was studied with operando PDF (Fig. 4h). A series of PDF patterns were collected while an NLNMO AMPIX cell was charged to 4.4 V and discharged to 2.0 V. The peak positions of different local bonding species evolve distinctly during cycling. The bond length of M–M bonds (M = Na, Li, Ni, Mn) decreases during charge and increases during discharge, which is in good agreement with the decreased lattice parameter *a* observed in sXRD. The decrease of M–M bond length during charge is primarily caused by the oxidation of TM ions, and this bond length increases during discharge as the TM ions are reduced. Similarly, the TM-O bond length is observed to decrease during charging and the bond length increases during discharging (TM = Ni, Mn, Li as here Li are within the TM layer). The potential contribution of oxygen redox was also investigated with the changes of Na–O bond length in operando PDF. In the charge process, an increase of Na–O bond length was initially observed, followed by a slight decrease at the end of the charge. The initial increase of Na–O bond length is caused by the reduced electrostatic attraction between oxygen and sodium ions with the

removal of positively charged sodium ions. At high voltage, the decrease of the Na–O bond length can be explained by the oxidation of the oxygen ions, as this increases the electrostatic attraction between oxygen and sodium ions. During discharge, the Na–O bond length slightly increases in the beginning, followed by a continual decrease until the end of discharge. The oxidized lattice oxygen could initially be reduced, which leads to a decrease of electrostatic attraction between oxygen and sodium ions, until enough sodium ions intercalate back into the structure to provide increased attraction. It is noticeable that the changes of Na–O bond length in PDF are remarkably similar to the changes of the *c* lattice in sXRD. The changes in the Na–O bond length in PDF matches well with our analysis of the pre-edge intensity changes of O K-edge in XAS and with the proposed oxygen redox activity at high voltage.

The higher energy region of XAS, known as extended X-ray absorption fine structures (EXAFS), can provide information about both the local structure and oxidation states of the irradiated material. Herein, the Fourier transformed EXAFS spectra for NLNMO (Fig. 5a, 5b) at Mn and Ni K-edges are studied to quantify the changes of Ni and Mn local ordering. EXAFS analysis is a powerful method to determine the local interatomic distances in TM oxides, and the best-fit values of the structure parameters used for NLNMO are listed in Tables I and II. In Mn and Ni K-edge EXAFS spectra, the first intense peak corresponds to the TM-O distance in the first coordination sphere and the second intense peak correspond to the TM-TM distance (Figs. 5c–5e). The magnitudes of the TM-O and TM-TM bonds for both Mn K-edge and Ni K-edge are compared and shown in SI Fig. 3 with blue lines as guides. The Mn-O peak has a larger magnitude than the Mn-TM peak whereas the Ni–O peak has a smaller magnitude than the Ni-TM peak. Ni and Mn have higher electron backscattering ability than Li because they have higher atomic numbers. Since the Mn-TM peak has a smaller magnitude than Ni-TM peak, it is inferred that Mn atoms typically surround Li atoms in the TM layer. Ni atoms may be mostly surrounded by other Ni atoms and Mn atoms, which increases the magnitude of the Ni-TM peak. The preferred transition metal positioning observed in the EXAFS data is corroborated by the findings in the sXRD data. The Mn atoms surrounding Li atoms can together form the partially ordered LiMn$_6$ honeycomb structures,[54] which lead to the superlattice peak observed in sXRD. TM layer ordering in 4d TM sodium cathodes has been shown to alter the oxygen bonding to trigger oxygen redox.[47] This same phenomenon can be seen for the NLNMO reported here for 3d TM sodium cathodes, enabling a new route for oxygen redox.

In the charge process, as sodium is extracted from the crystal lattice, the first coordination Ni–O interatomic distance changes clearly whereas the Mn-O distance has negligible changes. The Ni–O interatomic distance decreases during charge to 4.2 V, representing the Ni oxidation during charge. From 4.2 V to 4.4 V, the Ni–O interatomic spacing increases, which implies a slight reduction of Ni oxidation state at high voltage, thus indicating a different reaction pathway related to oxygen activity. After discharge to 2.0 V, the Ni–O interatomic distance exhibits little change compared to the pristine state, showing that the Ni oxidation is mostly reversible. This is in good agreement with the data from the XANES spectrum that Ni redox reaction is reversible whereas Mn remains inactive during charge and discharge. The TM ordering within the TM layer can be evaluated by the Debye-Waller factor (σ) as well as the peak intensity of Ni–O and Mn–O peaks in EXAFS. The Debye-Waller factor (σ) reflects the random thermal and static vibrations of the absorbing atoms around their equilibrium atomic positions. Larger values of the Debye-Waller factor are a result of structure distortions that deviate from the ideal model.[55] As displayed in Tables I and II, the Debye-Waller factor increases for TM-O during charging, which indicates structure distortion of the TM-O bond. Specifically, the Ni–O Debye-Waller factor increases significantly during charging, indicating that the NiO$_6$ octahedron distorts more than the MnO$_6$ bond during cycling. This increased distortion during charging may signify a change in Ni–O covalency

through the creation of unsymmetrical oxygen bonds. This distortion could also be caused by the migration of Ni from its pristine state. The peak intensity of Ni–O and Mn-O peak in EXAFS are also compared in SI Fig. 3, where a drop of peak intensity in TM-O bond is seen at high voltage, especially for the Ni–O case. The peak height is highly dependent on the system ordering; thus, the large drop of Ni–O peak intensity indicates severe disruption of the local TM-O honeycomb ordering, which can result from the TM migration.

To further explore the local TM migration and the effect of the loss of TM ordering, density of states (DOS) were calculated for NLNMO at fully charged state with and without Ni migration (Fig. 5f, 5g) and SI Fig. 4. At high voltage, undercoordinated oxygen can lead to a slight reduction of TM. This can induce electron transfer from the O to the TM, causing O$_2$ gas release along with the reduction of TM.[34] Oxygen gas release has been reported during the high voltage region in other Ni containing oxygen redox active cathodes.[56] TM reduction is also observed in our Ni XAS results where Ni is reduced from 4.2 to 4.4 V. After Ni migration, there is a reduction of the number of unoccupied oxygen states above the Fermi level (Figs. 5f, 5g), SI Fig. 4. This can inhibit oxygen reduction upon cell discharge, resulting in irreversibility during the first cycle. The combination of oxygen loss and Ni migration can result in irreversible oxygen redox activity that will lead to reduced capacity in the following discharge.[57]

This experimental study of the origin of the irreversible oxygen redox activity combined with information gleaned through literature review, reveals that the inclusion of Ni is detrimental to the reversibility of oxygen redox at high voltage in NIBs. The inclusion of Ni may enable irreversible O$_2$ gas release, and Ni migration within the structure can alter the bonding environment of oxygen so that it is not favorable for further oxygen redox activity. To mitigate O$_2$ gas release, other TMs, such as Fe, should be included to enhance TM-O hybridization.[56] Unlike LIB cathode materials, the inclusion of Ni in sodium cathodes that exhibit oxygen redox due to TM ordering should be carefully managed to optimize the reversibility of oxygen redox activity at high voltage.

Conclusions

Meso-structured controlled P2-type Na$_{0.8}$Li$_{0.12}$Ni$_{0.22}$Mn$_{0.66}$O$_2$ (NLNMO) was synthesized by meso-structure controlled carbonate co-precipitation with transition metal layer ordering in the pristine structure as confirmed by sXRD and EXAFS. NLNMO, synthesized in this study, has a rate dependent plateau during the first charge, which likely indicates oxygen redox activity. To evaluate the redox activities of NLNMO at high voltage, ex situ XAS was used to observe the O K-edge, Ni K-edge, and Mn K-edge during the first electrochemical cycle. An increase in the O pre-edge integrated intensity was observed from 4.2 V–4.4 V whereas the Mn K-edge shifted negligibly, and Ni was reduced in this voltage range. This indicates that oxygen redox activity is responsible for the plateau at high voltage during the first charge. After the first charge, the plateau disappears and will not appear in the following cycles: the super-lattice peak observed in sXRD also diminish after first cycle, indicating loss of ordering in the TM layer. Ni migration was studied through EXAFS and DOS and is considered to be responsible for the loss of TM layer ordering and the decrease of available states in oxygen above Fermi level. This change of oxygen environment, along with O$_2$ gas production, is likely the cause of the irreversibility of oxygen redox. Through this work we demonstrated that the inclusion of Ni in sodium cathodes is detrimental to the reversibility of oxygen redox at high voltage. This work emphasizes the importance of TM layer ordering on inducing oxygen redox activity and reveals the unfavorable effect that Ni has on its reversibility. As such, future compositional design of sodium cathodes should avoid adoption of high Ni content in order to enhance reversible oxygen redox and achieve energy-dense and long-lasting sodium cathodes.
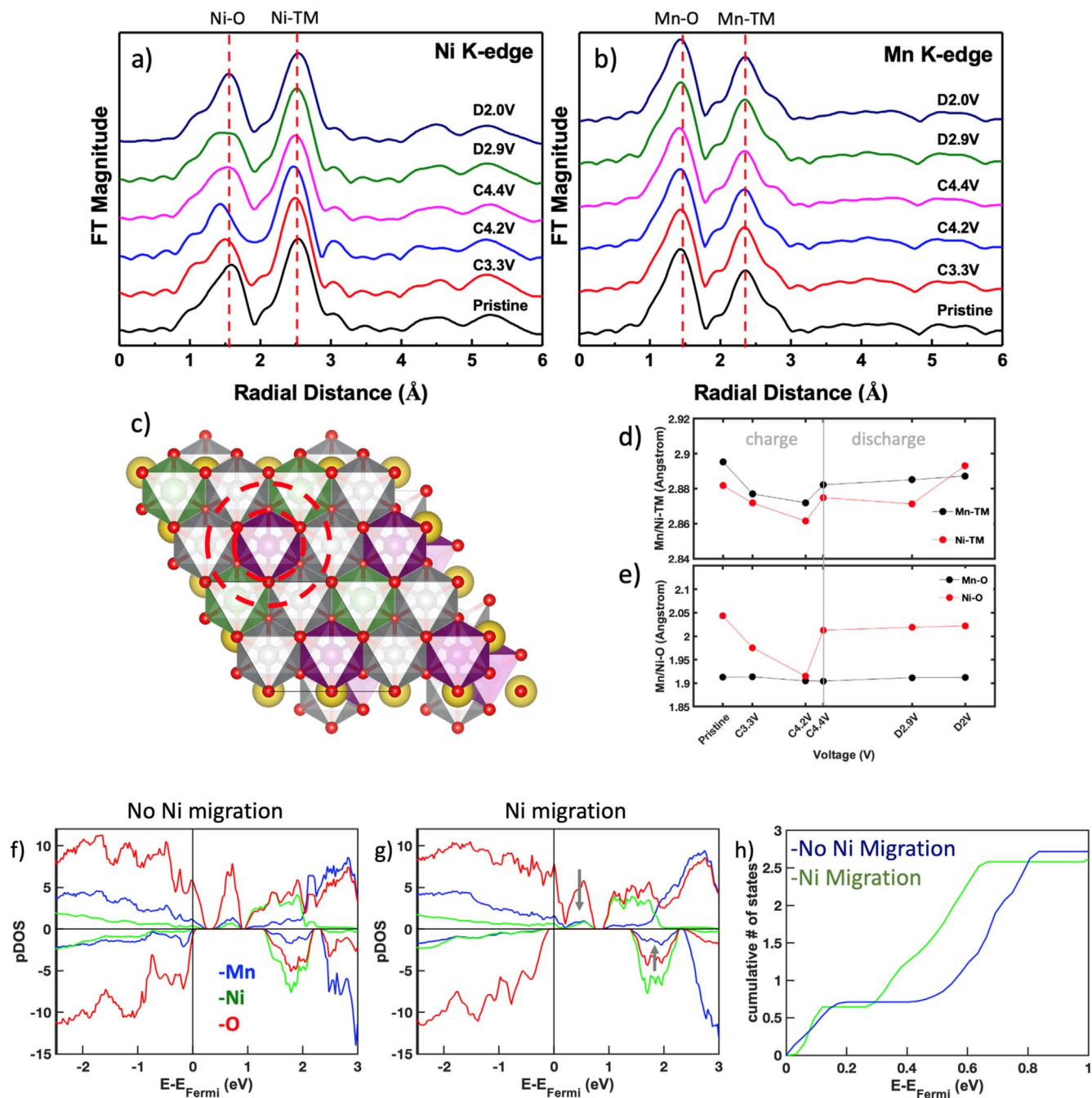
Figure 5. Ex situ EXAFS spectra of NLNMO at (a) Ni K-edge and (b) Mn K-edge at different states of charge. (c) A model of the crystal structure of NLNMO with the first two nearest neighbors starting from the atom centered in the circled in dashed red lines. (d) The bond length of Mn/Ni-TM and the (e) bond length of Mn/Ni–O at different states of charge. The black points represent the Mn– bonds while the red points represent the Ni– bonds. DOS near the Fermi level for fully charged NLNMO with (f) no Ni migration and (g) with Ni migration. (h) The cumulative number of unoccupied oxygen states above the Fermi level.

Table I. *Ex situ* EXAFS fit results for sample collected at the Mn K-edge. The phase-corrected bond length (R) and Debye-Waller factor (s^2) are shown for each interaction.

Sample	Pristine	c3.3 V	c4.2 V	c4.4 V	d2.9 V	d2.0 V
R_{Mn-O} (Å)	1.913	1.913	1.904	1.904	1.912	1.912
R_{Mn-TM} (Å)	2.895	2.877	2.872	2.882	2.885	2.887
$\sigma_{Mn-O} \times 10^{-3}$	3.5	3.8	4.1	4.5	3.5	3.6
$\sigma_{Mn-TM} \times 10^{-3}$	4.4	4.6	5.1	5.6	4.5	4.6

k-range: 2.566–13.167, R-range: 0.873–3.085.

Table II. *Ex situ* EXAFS fit results for samples collected at the Ni K-edge. The phase-corrected bond length (R) and Debye-Waller factor (s^2) are shown for each interaction.

Sample	Pristine	c3.3 V	c4.2 V	c4.4 V	d2.9 V	d2.0 V
R_{Ni-O1} (Å)	2.043	1.975	1.9148	2.0127	2.019	2.022
R_{Ni-TM} (Å)	2.882	2.872	2.861	2.875	2.871	2.893
R_{Ni-O2} (Å)	3.361	3.356	3.414	3.378	3.343	3.358
σ_{Ni-O1} x 10^{-3}	6.3	10.3	11.0	10.2	11.0	6.7
σ_{Ni-TM} x 10^{-3}	5.6	5.0	5.3	6.2	5.3	5.7
σ_{Ni-O2} x 10^{-3}	4.8	3.9	5.0	6.5	5.1	4.9

k-range: 2.566–13.167, R-range: 1.169–3.420.

ORCID

Hayley Hirsh https://orcid.org/0000-0002-8105-6975
Ying Shirley Meng https://orcid.org/0000-0001-8936-8845

References

1. B. Dunn, B. Dunn, H. Kamath, and J. Tarascon, *Sci. Mag.*, **334**, 928 (2011).
2. Y. Jiang, Z. Yang, W. Li, L. Zeng, F. Pan, M. Wang, X. Wei, G. Hu, L. Gu, and Y. Yu, *Adv. Energy Mater.*, **5**, 1500091 (2015).
3. J. Z. Guo, X. L. Wu, F. Wan, J. Wang, X. H. Zhang, and R. S. Wang, *Chem. - A Eur. J.*, **21**, 17371 (2015).
4. Y. You, X. L. Wu, Y. X. Yin, and Y. G. Guo, *Energy Environ. Sci.*, **7**, 1643 (2014).
5. J. Song, L. Wang, Y. Lu, J. Liu, B. Guo, P. Xiao, J. J. Lee, X. Q. Yang, G. Henkelman, and J. B. Goodenough, *J. Am. Chem. Soc.*, **137**, 2658 (2015).
6. F. Wan, X. L. Wu, J. Z. Guo, J. Y. Li, J. P. Zhang, L. Niu, and R. S. Wang, *Nano Energy*, **13**, 450 (2015).
7. A. K. Padhi, K. S. Nanjundaswamy, and J. B. Goodenough, *J. Electrochem. Soc.*, **144**, 1 (1997).
8. H. S. Hirsh, Y. Li, D. H. S. Tan, M. Zhang, E. Zhao, and Y. S. Meng, *Adv. Energy Mater.*, **10**, 2001274 (2020).
9. Y. Sun, S. Guo, and H. Zhou, *Adv. Energy Mater.*, **9**, 1800212 (2019).
10. B. M. De Boisse, D. Carlier, M. Guignard, and C. Delmas, *J. Electrochem. Soc.*, **160**, 569 (2013).
11. M. H. Han, B. Acebedo, E. Gonzalo, P. S. Fontecoba, S. Clarke, D. Saurel, and T. Rojo, *Electrochim. Acta*, **182**, 1029 (2015).
12. N. A. Katcho, J. Carrasco, D. Saurel, E. Gonzalo, M. Han, F. Aguesse, and T. Rojo, *Adv. Energy Mater.*, **7**, 1 (2017).
13. C. Delmas, J.-J. Braconnier, C. Fouassier, and P. Hagenmuller, *Solid State Ionics*, **3–4**, 165 (1981).
14. Y. Guo, J. Zhang, J.-Z. Guo, W. Pang, X. Wu, Q. Yang, P. Wang, Z. Chen, and K. Huang, *ACS Appl. Mater. Interfaces*, **10**, 34272 (2018).
15. P. He, H. Yu, D. Li, and H. Zhou, *J. Mater. Chem.*, **22**, 3680 (2012).
16. K. Luo et al., *Nat. Chem.*, **8**, 684 (2016).
17. A. J. Perez, Q. Jacquet, D. Batuk, A. Iadecola, M. Saubanère, G. Rousse, D. Larcher, H. Vezin, M.-L. Doublet, and J.-M. Tarascon, *Nat. Energy*, **2**954 (2017).
18. G. Assat and J. M. Tarascon, *Nat. Energy*, **3**, 373 (2018).
19. N. Yabuuchi, *Chem. Lett.*, **46**, 412 (2017).
20. J. Hong, H. D. Lim, M. Lee, S. W. Kim, H. Kim, S. T. Oh, G. C. Chung, and K. Kang, *Chem. Mater.*, **24**, 2692 (2012).
21. E. McCalla et al., *Science (80-.)*, **350**, 1516 (2015).
22. M. Okubo and A. Yamada, *ACS Appl. Mater. Interfaces*, **9**, 36463 (2017).
23. D.-H. Seo, J. Lee, A. Urban, R. Malik, S. Kang, and G. Ceder, *Nat. Chem.*, **8**, 692 (2016).
24. A. Konarov, J. H. Jo, J. U. Choi, Z. Bakenov, H. Yashiro, J. Kim, and S. T. Myung, *Nano Energy*, **59**, 197 (2019).
25. K. Luo et al., *J. Am. Chem. Soc.*, **138**, 11211 (2016).
26. B. Li and D. Xia, *Adv. Mater.*, **29**, 1701054 (2017).
27. X. Rong et al., *Joule*, **2**, 125 (2018).
28. F. Meng et al., *Joule*, **3**, 503 (2018).
29. P.-F. Wang et al., *Nano Energy*, **69**, 104474 (2020).
30. U. Maitra et al., *Nat. Chem.*, **10**, 288 (2018).
31. Y. Li et al., *Adv. Energy Mater.*, **9**, 1803087 (2019).
32. C. Ma, J. Alvarado, J. Xu, R. J. Clément, M. Kodur, W. Tong, C. P. Grey, and Y. S. Meng, *J. Am. Chem. Soc.*, **139**, 4835 (2017).
33. C. Zhao, Q. Wang, Y. Lu, L. Jiang, L. Liu, X. Yu, L. Chen, B. Li, and Y. S. Hu, *Energy Storage Mater.*, **20**, 395 (2019).
34. Q. Jacquet, A. Iadecola, M. Saubanère, H. Li, E. J. Berg, G. Rousse, J. Cabana, M. L. Doublet, and J. M. Tarascon, *J. Am. Chem. Soc.*, **141**, 11452 (2019).
35. W. E. Gent et al., *Nat. Commun.*, **8**2091 (2017).
36. Y. Li, M. J. Zuba, S. Bai, Z. W. Lebens-Higgins, B. Qiu, S. Park, Z. Liu, M. Zhang, L. F. J. Piper, and Y. S. Meng, *Energy Storage Mater.*, **35**, 99 (2021).
37. L. B. Mccusker, R. B. Von Dreele, D. E. Cox, D. Louër, and P. Scardi, *J. Appl. Crystallogr.*, **32**, 36 (1999).
38. C. L. Farrow, P. Juhas, J. W. Liu, D. Bryndin, E. S. Boin, J. Bloch, T. Proffen, and S. J. L. Billinge, *J. Phys. Condens. Matter,*, **19.33**, 335219 (2007).
39. D. Joubert, *Phys. Rev. B - Condens. Matter Mater. Phys.*, **59**, 1758 (1999).
40. J. P. Perdew, K. Burke, and M. Ernzerhof, *Phys. Rev. Lett.*, **77**, 3865 (1996).
41. A. Jain et al., *APL Mater.*, **1**, 011002 (2013).
42. R. A. House et al., *Chem. Mater.*, **31**, 3293 (2019).
43. J. Xu, D. H. Lee, R. J. Clément, X. Yu, M. Leskes, A. J. Pell, G. Pintacuda, X. Q. Yang, C. P. Grey, and Y. S. Meng, *Chem. Mater.*, **26**, 1260 (2014).
44. A. R. Armstrong et al., *JACS*, **128**, 8694 (2006).
45. Y. Wang, R. Xiao, Y. S. Hu, M. Avdeev, and L. Chen, *Nat. Commun.*, **6**, 6954 (2015).
46. R. D. Shannon, *Acta Crystallogr., Sect. A*, **32**, 751 (1976).
47. B. Mortemard de Boisse et al., *Nat. Commun.*, **7**, 11397 (2016).
48. F. M. E. DeGroot, M. Grioni, J. C. Fuggle, J. Ghijsen, and G. A. Sawatzky, *Phys. Rev. B*, **40**, 5715 (1989).
49. T. Kroll, M. Knupfer, J. Geck, C. Hess, T. Schwieger, G. Krabbes, C. Sekar, D. R. Batchelor, H. Berger, and B. Büchner, *Phys. Rev. B*, **74**, 115123 (2006).
50. X. Bai, M. Sathiya, B. Mendoza-Sánchez, A. Iadecola, J. Vergnet, R. Dedryvère, M. Saubanère, A. M. Abakumov, P. Rozier, and J. M. Tarascon, *Adv. Energy Mater.*, **8**, 1802379 (2018).
51. Z. Lu, L. Y. Beaulieu, R. A. Donaberger, C. L. Thomas, and J. R. Dahn, *J. Electrochem. Soc.*, **149**, A778 (2002).
52. E. de la Llave, P. K. Nayak, E. Levi, T. R. Penki, S. Bublil, P. Hartmann, F.-F. Chesneau, M. Greenstein, L. F. Nazar, and D. Aurbach, *J. Mater. Chem. A*, **5**, 5858 (2017).
53. D. Kim, S. H. Kang, M. Slater, S. Rood, J. T. Vaughey, N. Karan, M. Balasubramanian, and C. S. Johnson, *Adv. Energy Mater.*, **1**, 333 (2011).
54. J. Bréger, N. Dupré, P. J. Chupas, P. L. Lee, T. Proffen, J. B. Parise, and C. P. Grey, *J. Am. Chem. Soc.*, **127**, 7529 (2005).
55. M. Cao, Z. Shadike, Y. Zhou, and Z. Fu, *Electrochim. Acta*, **295**, 918 (2019).
56. Y. Zhang, M. Wu, J. Ma, G. Wei, Y. Ling, R. Zhang, and Y. Huang, *ACS Cent. Sci.*, **6**, 232 (2020).
57. M. Ben Yahia, J. Vergnet, M. Saubanère, and M. L. Doublet, *Nat. Mater.*, **18**, 496 (2019).